Supplementary material

Lithospheric transdimensional ambient noise tomography of W-Europe: implications for crustal scale geometry of the W-Alps

A. Nouibat[1], L. Stehly[1], A. Paul[1], S. Schwartz[1], T. Bodin[2], T. Dumont[1], Y. Rolland[1,3], R. Brossier[1], Cifalps Team and AlpArray Working Group

[1] Univ. Grenoble Alpes, Univ. Savoie Mont Blanc, CNRS, IRD, UGE, ISTerre, *38000 Grenoble, France.*

[2] Univ. Lyon, UCBL, CNRS, LGL-TPE, *69622 Villeurbanne, France.*

[3] Univ. Savoie Mont Blanc, CNRS, UMR 5204, EDYTEM, *73370 Le Bourget-du-Lac, France.*

1 Distance-time plot of noise correlations

Fig. S1 shows a distance-time section of vertical-component seismic ambient noise cross-correlations computed in a region including most of the Western Alps. The dispersive Rayleigh wave emerges very clearly with a fairly good symmetry between the causal and acausal parts.

2 Comparison of the 8-s and 25-s group-velocity maps with sedimentary basins and Moho depth maps

Figure S2(a) shows the 8-s group-velocity map together with main sedimentary basins. Figure S2(b) shows the 25-s group-velocity map with contours of the reference Moho depth model of Spada et al. (2013), that is mainly derived from controlled-source seismology (CSS) and receiver-function data. The thick crust of the Alps and the Apennines mountain belts coincides with areas of low velocity < 3.0 km/s. Areas of thin crust such as the Liguro-Provençal basin and the Tyrrhenian Sea coincide with high velocity anomalies > 3.4 km/s .

3 Comparison with a matrix-based inversion

We compared results of the *rj-McMC* algorithm with a matrix-based linearized inversion (Boschi & Dziewonski., 1999) for the same dataset at 15 s period (Fig. S3). The linear problem is solved using an iterative *LSQR* algorithm (Paige and Saunders., 1982). The model solution is computed using an adaptive grid-based path density that remains fixed during inversion (Schaefer et al., 2011; Lu et al., 2018; Fig. S3(a)). Cell sizes of 0.15°, 0.3° and 0.6° were used depending on the path density (Fig. S3(b)). The regularization coefficients (damping, roughness) were set according to the maximum curvature of the *L-curve*. Fig. S3(c) shows the *rj-McMC* solution model computed by averaging the ensemble of models obtained from 64 Markov chains in parallel after 180×10^3 steps. The posterior map of velocity uncertainties is generated by computing the variance of this ensemble (Fig. S3(d)). The image resulting from the *rj-McMC* inversion is not as smooth as the one resulting from the linearized inversion, which is affected by the imposed degree of smoothing. On the other hand, a stronger velocity contrast is obtained using the trans-D inversion, with more focused anomalies that suggest a better resolution (see for example the low-velocity anomaly in the Po plain). In addition, the trans-D inversion highlights new features such as the high-velocity anomaly at 4° longitude and 43.5° latitude.

4 Posterior distribution on the number of Voronoi cells

Figure S4 shows the posterior probability distribution on the number of Voronoi cells used to describe the 2-D velocity field in the *rj-McMC* tomography shown in Fig. S3(c). The small standard deviation of the Gaussian-shaped probability density curve shows that the algorithm has converged. The maximum model solution occurs for $760 - 770$ Voronoi cells.

5 Inversion misfit

Figure S5(a) shows the evolution of the normalized model misfit function with the number of iterations in the *rj-McMC* inversion shown in Fig. S3(c). The misfit reduction reaches $\sim 90\%$. The posterior histogram of traveltime misfit between model predictions and observations is shown in Fig. S5(b).

6 Checkerboard tests

In Fig. S6, we check the resolution power of the *rj-McMC* inversion by synthetic checkerboard tests for cell sizes of 1° and 2°. Figures S6(1a)-(2a) show input models with square-shaped anomalies. Synthetic travel times were computed using the same source and receiver geometry as in observations at 15 s period, with added random Gaussian noise of 1 s standard deviation. Figures S6(1b)-(2b) show the average solution models obtained from the *rj-McMC* tomography. The Hierarchical Bayes reversible jump method is able to recover the velocity areas as defined in the synthetic models.

7 Depth sections through the V_s model along reference profiles

In Fig. S7, we present depth sections along three reference profiles across the Alpine mountain range: Cifalps and ECORS-CROP in the Western Alps and the alpine part of the EASI N-S transect in the Eastern Alps.

8 Comparison with the V_s model by Zhao et al. (2020)

Fig. S8 shows a comparison between our V_s model and the one by Zhao et al. (2020) on depth sections along the Cifalps and ECORS-CROP profiles. To facilitate the comparison between the results of the two models, we added on each depth section the reference Moho depth model of Spada et al. (2013) and the 4.3 km/s iso-velocity contour that we use as a proxy for the Moho (see discussion in section 5.2 of the main text). The middle and lower crust of the western parts of both profiles have higher velocities in our model than in Zhao et al. (2020). This difference is most probably due to the improved data coverage in our dataset with respect to the one of Lu et al. (2018) used in the inversion of Zhao et al. (2020), in particular in the westernmost part of the AlpArray network. In the alpine part of the Cifalps section, the model by Zhao et al. (2020) and our model exhibit similar first order features. In particular, they exhibit consistent geometries of the Ivrea body and similar Moho depths.

By contrast, these two models exhibit striking differences along the ECORS-CROP transect. The depth of the 4.3 km/s iso-velocity in our model is consistent with the Moho depth of Spada et al. (2013), but is deeper in Zhao et al. (2020). The 3.8 km/s V_s contour would better fit the Moho model of Spada et al. (2013), although 3.8 km/s is rather low for a Moho proxy.

Another striking difference is the velocity gradient at the Moho, which is strong in our model and smooth in Zhao et al. (2020). Our strong gradient is more in line with the results of receiver functions studies (Zhao et al., 2015) and seismic reflection profiling (e.g. ECORS-CROP Deep Seismic Sounding Group, 1989; Thouvenot et al., 2007) in the Western Alps, which documented a highly reflective Moho. This strong velocity gradient at Moho depth in our model is a direct consequence of the chosen parameterization and the 4-layer model assumption. By contrast, the reference model in the transdimensional inversion of Zhao et al. (2020) is a homogeneous half-space of 3.8 km/s velocity.

References

Boschi, L. and Dziewonski, A. M. (1999). High- and low-resolution images of the Earth's mantle: Implications of different approaches to tomographic modeling. *Journal of Geophysical Research: Solid Earth*, 104(B11):25567–25594.

Hetényi, G., Plomerová, J., Bianchi, I., Kampfová Exnerová, H., Bokelmann, G., Handy, M. R., and Babuška, V. (2018). From mountain summits to roots: Crustal structure of the eastern alps and bohemian massif along longitude 13.3°e. *Tectonophysics*, 744:239–255.

Hirn, A., Nadir, S., Thouvenot, F., Nicolich, R., Pellis, G., Scarascia, S., Tabacco, I., Castellano, M., and Merlantip, F. (1989). A new picture of the Moho under the western Alps. *Nature*, 337:249–251.

Lu, Y., Stehly, L., Paul, A., and AlpArray Working Group (2018). High-resolution surface wave tomography of the European crust and uppermost mantle from ambient seismic noise. *Geophysical Journal International*, 214(2):1136–1150.

Paige, C. C. and Saunders, M. A. (1982). LSQR: An Algorithm for Sparse Linear Equations and Sparse Least Squares. *ACM Trans. Math. Softw.*, 8(1):43–71.

Schaefer, J. F., Boschi, L., and Kissling, E. (2011). Adaptively parametrized surface wave tomography: methodology and a new model of the European upper mantle. *Geophysical Journal International*, 186(3):1431–1453.

Spada, M., Bianchi, I., Kissling, E., Agostinetti, N. P., and Wiemer, S. (2013). Combining controlled-source seismology and receiver function information to derive 3-D Moho topography for Italy. *Geophysical Journal International*, 194(2):1050–1068.

Thouvenot, F., Paul, A., Fréchet, J., Béthoux, N., Jenatton, L., and Guiguet, R. (2007). Are there really superposed Mohos in the southwestern Alps? New seismic data from fan-profiling reflections. *Geophysical Journal International*, 170(3):1180–1194.

Zhao, L., Malusà, M. G., Yuan, H., Paul, A., Guillot, S., Lu, Y., Stehly, L., Solarino, S., Eva, E., Lu, G., and Bodin, T. (2020). Evidence for a serpentinized plate interface favouring continental subduction. *Nature Communications*, 11:2171.

Zhao, L., Paul, A., Guillot, S., Solarino, S., Malusà, M., Zheng, T., Salimbeni, S., Dumont, T., Schwartz, S., Zhu, R., and Wang, Q. (2015). First Seismic Evidence for Continental Subduction beneath the Western Alps. *Geology*, 43:815–818.

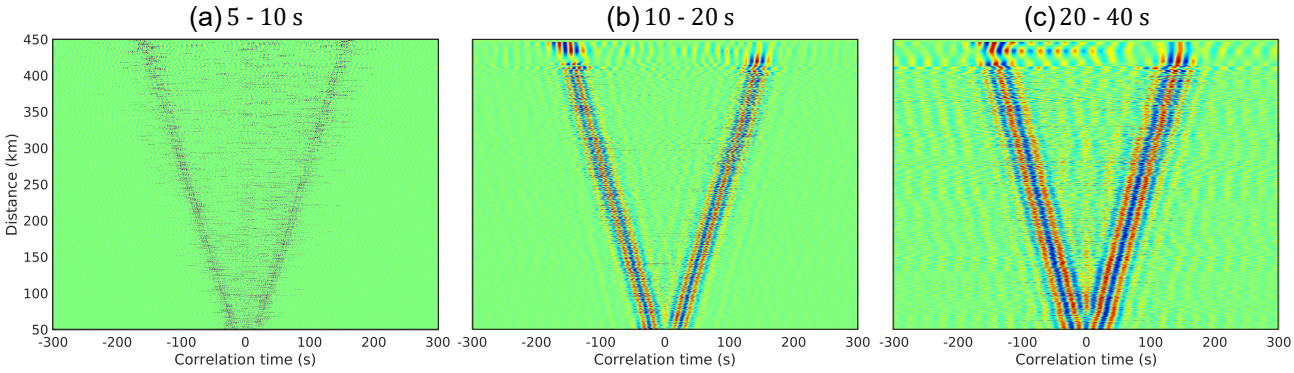

Figure S1. Sections of noise cross-correlation traces in the $5-10$ s, $10-20$ s and $20-40$ s period bands. The trace amplitudes are normalized to one. The causal part (positive times) corresponds to Rayleigh waves propagating eastwards while the acausal part (negative times) corresponds to Rayleigh waves propagating westwards.

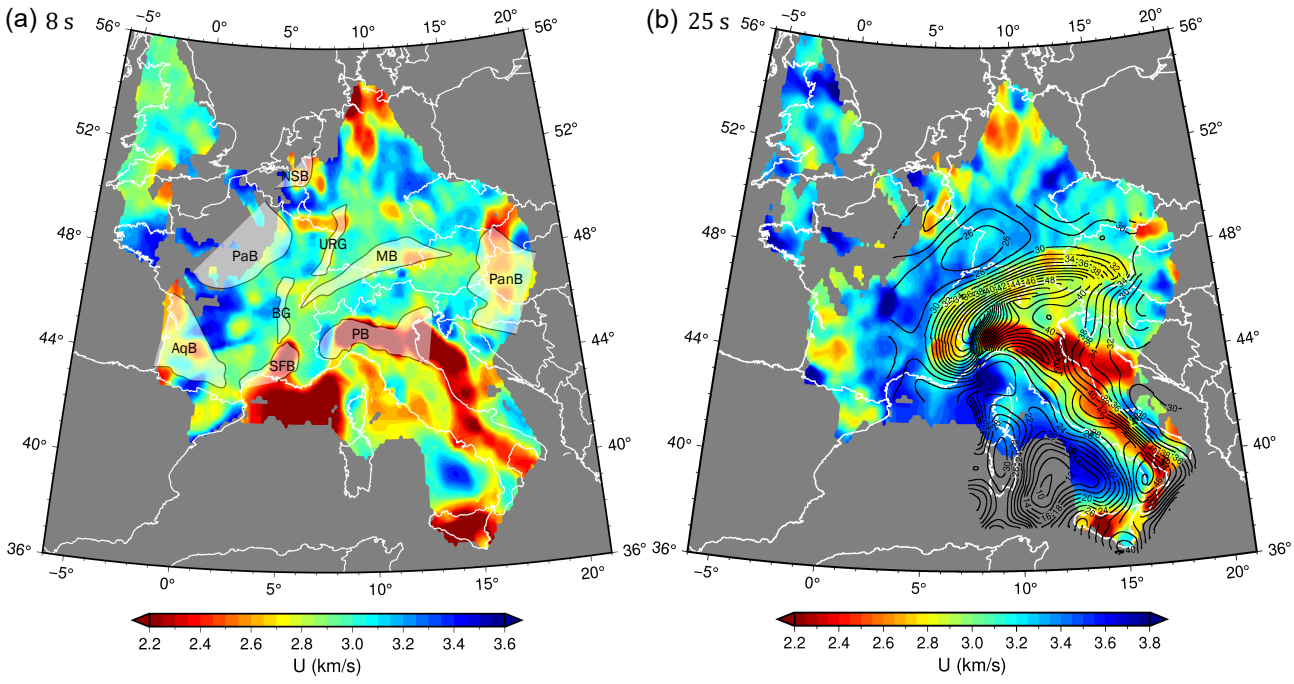

Figure S2. (a) Group-velocity map at 8 s period and Jurassic to Tertiary main sedimentary basins (shown as partially transparent areas). NSB: North-Sea basin, PB: Po basin, SFB: Southeast-France basin, AqB: Aquitaine basin, PaB: Paris basin, BG: Bresse Graben, URG: Upper Rhine Graben, MB: Molasse basin, PanB: Pannonian Basin. (b) Group-velocity map at 25 s period. Black lines are contours of the reference Moho depth map by Spada et al. (2013).

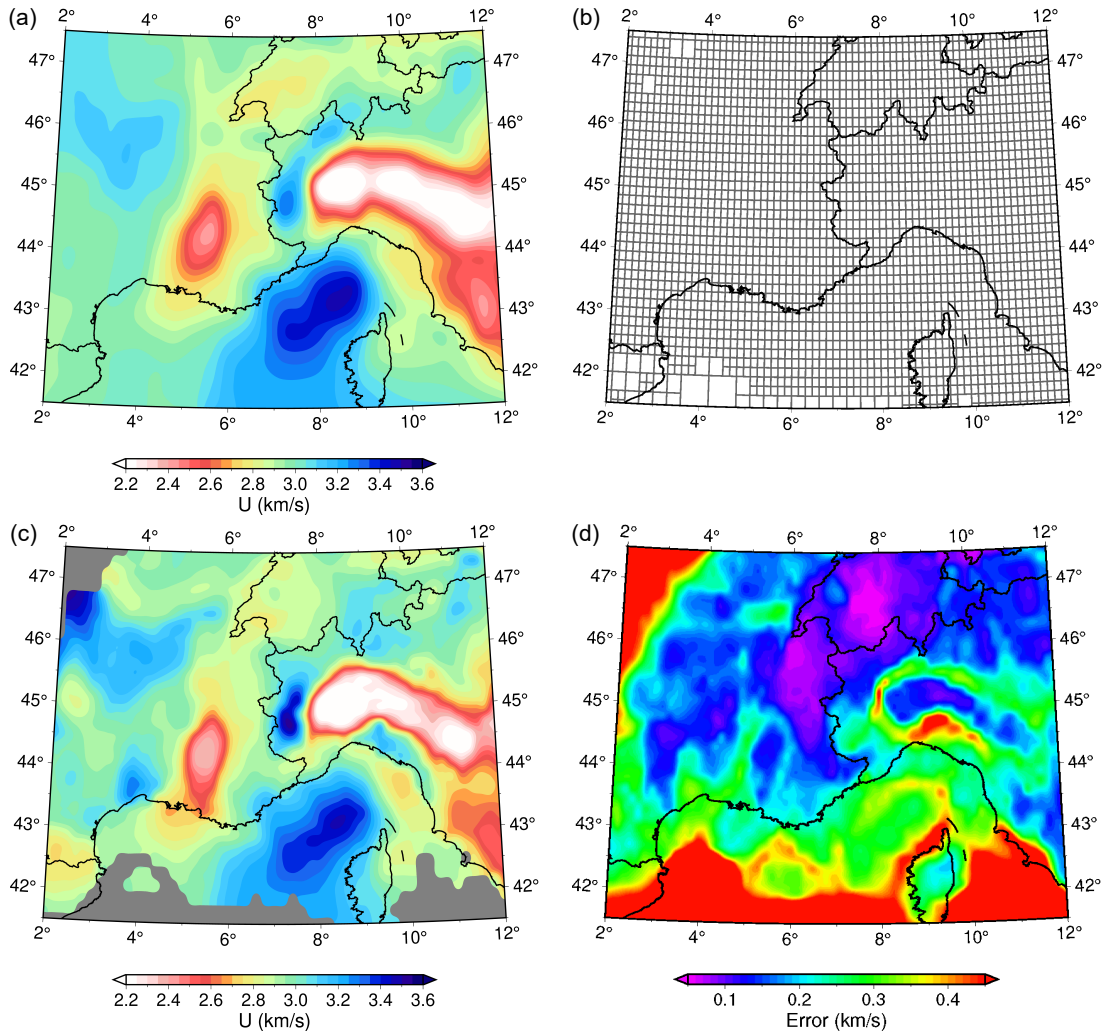

Figure S3. Comparison of the result of our Hierarchical Bayes inversion with the result of a matrix-based inversion at 15 *s* period. (a) Group-velocity map output of the regularized method. (b) Adaptive grid used to produce the regularized solution model. (c) Result of the Hierarchical Bayes reversible jump method. (d) Estimated error for the reversible jump tomography.

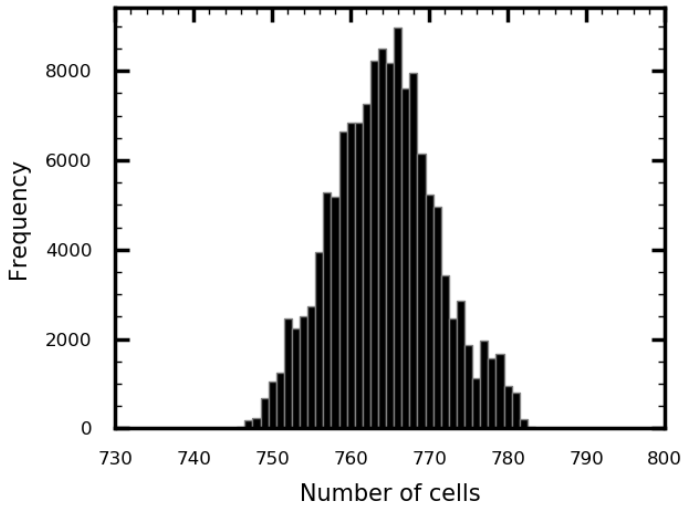

Figure S4. Posterior probability density for the number of Voronoi cells at 15 *s* period.

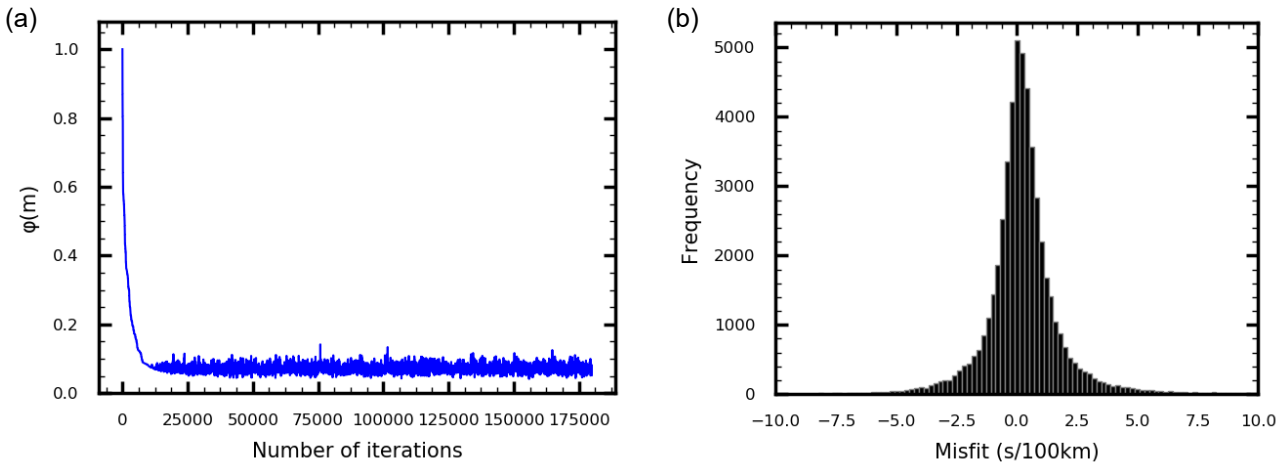

Figure S5. Misfit outputs at 15 *s* period from the reversible jump tomography. (a) Model misfit variation as a function of the number of iterations. (b) Histogram of traveltime misfit.

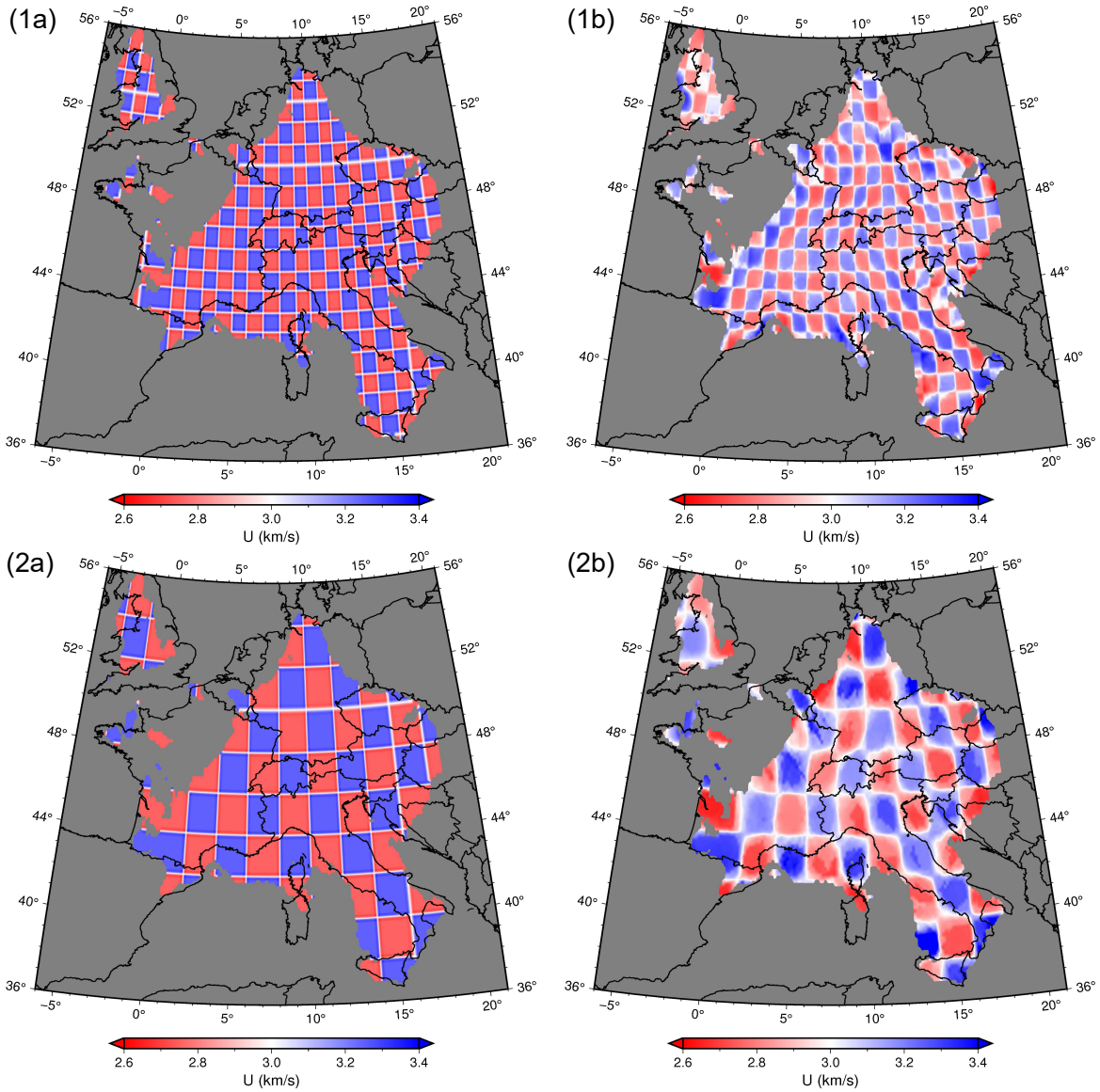

Figure S6. (1a) Input synthetic velocity model with a cell size of 1°. (1b) Average solution model of the Hierarchical Bayes reversible jump tomography. (2a) Input synthetic velocity model with a cell size of 2°. (2b) Average solution model of the Hierarchical Bayes reversible jump tomography.

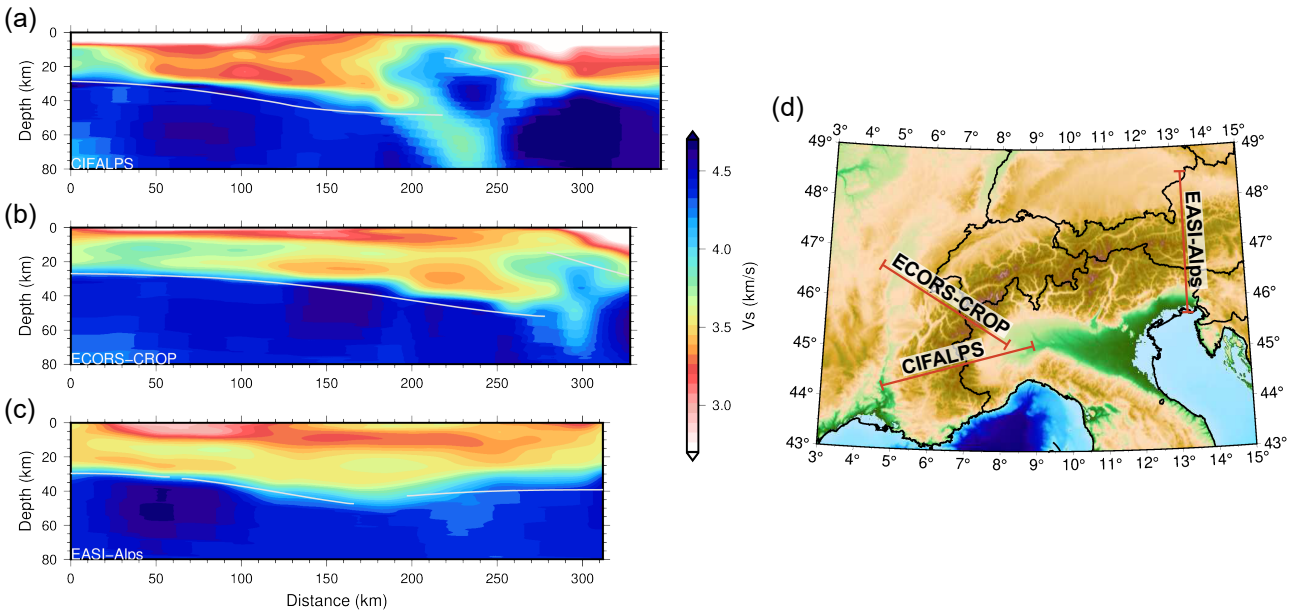

Figure S7. Cross sections in our V_s model along: a) the CIFALPS profile, b) the ECORS-CROP profile, and c) the alpine part of the EASI profile (Hetényi et al., 2018). The white lines show Spada et al. (2013)'s Moho depth model. (d) Location map of the three profiles.

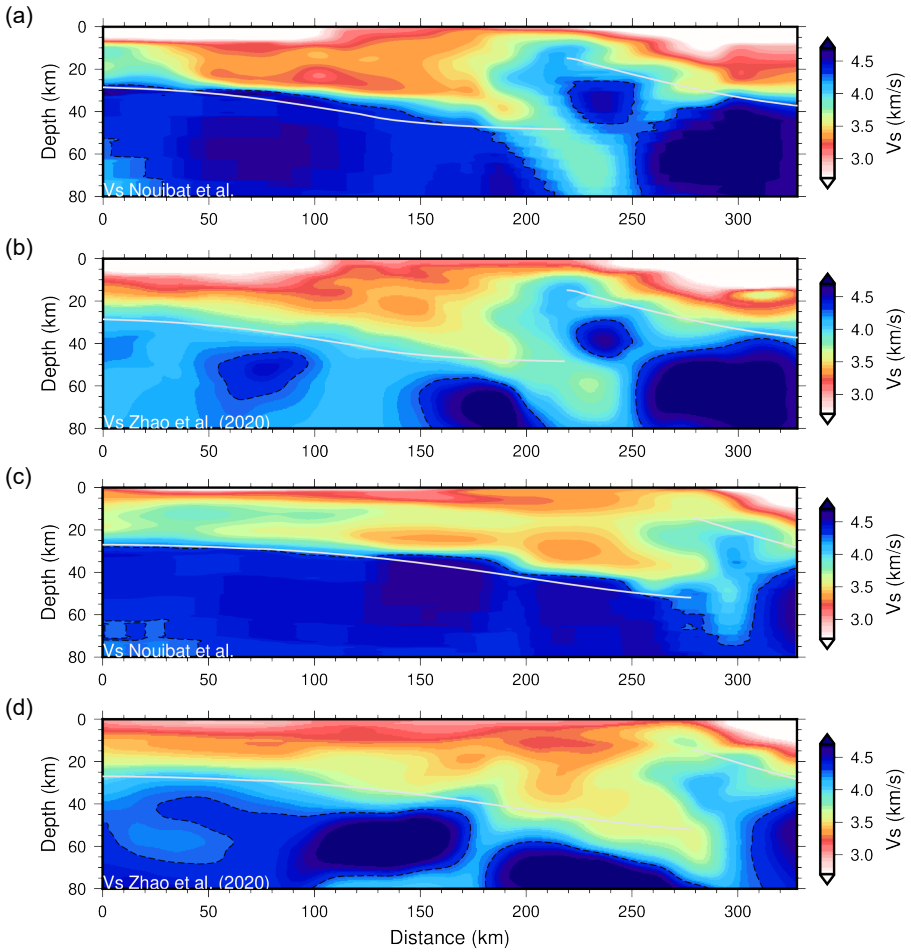

Figure S8. Cross sections in our V_s model and in the V_s model of Zhao et al. (2020), along the Cifalps (a, b) and ECORS-CROP (c, d) profiles. The dashed black lines correspond to the 4.3 km/s velocity contour. The thick white lines correspond to Spada et al. (2013)'s Moho depth.